energies

MDPI

Article

Flow Adjustment Inside and Around Large Finite-Size Wind Farms

Ka Ling Wu and Fernando Porté-Agel *

Wind Engineering and Renewable Energy Laboratory (WIRE), School of Architecture, Civil and Environmental Engineering (ENAC), École Polytechnique Fédérale de Lausanne (EPFL), EPFL-ENAC-IIE-WIRE, 1015 Lausanne, Switzerland; ka.wu@epfl.ch

* Correspondence: fernando.porte-agel@epfl.ch; Tel.: +41-21-693-6138

Received: 1 December 2017; Accepted: 14 December 2017; Published: 18 December 2017

Abstract: In this study, large-eddy simulations are performed to investigate the flow inside and around large finite-size wind farms in conventionally-neutral atmospheric boundary layers. Special emphasis is placed on characterizing the different farm-induced flow regions, including the induction, entrance and development, fully-developed, exit and farm wake regions. The wind farms extend 20 km in the streamwise direction and comprise 36 wind turbine rows arranged in aligned and staggered configurations. Results show that, under weak free-atmosphere stratification ($\Gamma = 1$ K/km), the flow inside and above both wind farms, and thus the turbine power, do not reach the fully-developed regime even though the farm length is two orders of magnitude larger than the boundary layer height. In that case, the wind farm induction region, affected by flow blockage, extends upwind about 0.8 km and leads to a power reduction of 1.3% and 3% at the first row of turbines for the aligned and staggered layouts, respectively. The wind farm wake leads to velocity deficits at hub height of around 3.5% at a downwind distance of 10 km for both farm layouts. Under stronger stratification ($\Gamma = 5$ K/km), the vertical deflection of the subcritical flow induced by the wind farm at its entrance and exit regions triggers standing gravity waves whose effects propagate upwind. They, in turn, induce a large decelerating induction region upwind of the farm leading edge, and an accelerating exit region upwind of the trailing edge, both extending about 7 km. As a result, the turbine power output in the entrance region decreases more than 35% with respect to the weakly stratified case. It increases downwind as the flow adjusts, reaching the fully-developed regime only for the staggered layout at a distance of about 8.5 km from the farm edge. The flow acceleration in the exit region leads to an increase of the turbine power with downwind distance in that region, and a relatively fast (compared with the weakly stratified case) recovery of the farm wake, which attains its inflow hub height speed at a downwind distance of 5 km.

Keywords: atmospheric boundary layer (ABL); boundary-layer depth; exit region; farm wake; induction region; large-eddy simulation (LES); large finite-size wind farm; turbulence

1. Introduction

Among all of the available renewable energy forms, wind energy is the fastest-growing electricity source on the globe. Much of the added wind power capacity comes from large-scale onshore and offshore wind farms. As the number and size of these large-scale wind farms continue to increase, it is of prime importance to understand the interaction between the atmospheric boundary layer (ABL) and wind farms. Various studies [1–7] have investigated the interaction between the ABL and very large wind farms (i.e., infinite wind farms). Inside such wind farms, the ABL flow reaches its asymptotic fully-developed regime, in which the power extraction of the wind turbines is balanced by the vertical turbulent transport of kinetic energy entrained from the flow above [2,4–9]. Lu and Porté-Agel, Johnstone and Coleman, and Abkar and Porté-Agel [4,6,7] demonstrated that such kinetic energy

entrainment results in an increase in the boundary-layer depth. They also showed that within very large wind farms, a stronger free-atmosphere stratification leads to a lower entrainment and boundary-layer depth, and thus a decrease in the power output of the farms. Abkar and Porté-Agel [10] later examined the mean and turbulent kinetic energy budgets of very large wind farms in a conventionally-neutral boundary layer (CNBL). Calaf et al. [2] proposed that such fully-developed regime could be established for ABL flows over wind farms whose length exceeds the height of the ABL by one order of magnitude.

For finite-size wind farms, or at the entrance and exit regions of large wind farms, the energy extracted by the wind turbines is balanced by both horizontal and vertical kinetic energy fluxes. To understand the complex interactions between the ABL and finite-size wind farms, several numerical simulation studies have been performed using large-eddy simulation (LES) [11–24]. Some of these studies have focused on validating the numerical simulation technique against field measurements in operational wind farms. For instance, Porté-Agel et al. [11] used LES to study the ABL flow through a wind farm located in Minnesota and showed a good prediction of the mean wind velocity profiles in the turbine wakes. Porté-Agel et al. [12], and Wu and Porté-Agel [14] performed LESs of the Horns Rev wind farm and compared the turbine power output data from the Horns Rev simulations to the field measurements reported by Barthelmie et al. [22,25], showing good agreement between the data sets. Churchfield et al. [17], Creech et al. [23], Eriksson et al. [18], and Nilsson et al. [19] showed that the simulated power production in the Lillgrund farm agrees well with field measurements and the overall wind farm efficiency is well predicted. The agreement between the results of the previously mentioned wind farm LESs and the field measurements demonstrated the robustness of the LES technique for the study of ABL flows and their interaction with wind farms.

Regarding the effects of atmospheric stability on finite-size wind farms, Abkar et al. [20], using LES, demonstrated that the performance of a finite-size wind farm varies over the course of a diurnal cycle due to the changes in ABL thermal stability and their effects on the turbine wakes and the associated power losses. Wake recovery and turbulent mixing are enhanced during the day as the positive buoyancy flux and the associated turbulence production result in a relatively high turbulence level in the ABL flow. Conversely, wakes recover more slowly during the night since the low turbulence intensity leads to a slow entrainment rate of momentum into the wake. Ghaisas et al. [24] studied the combining effect of atmospheric stability and wind farm configuration on finite-size wind farms through the use of LES and showed that the vertical mixing, horizontal spread and localized regions of acceleration caused by upstream turbine wake are responsible for turbine wake losses. Most of the other numerical studies performed on finite-size wind farms have focused on purely neutral pressure driven ABL flows. However, the ABLs observed in the atmosphere are seldom purely neutral, and the real ABLs that are identified as neutral are very often CNBLs capped by the stably-stratified free atmosphere [26].

Some recent studies have highlighted the importance of understanding and predicting the flow adjustment upwind (induction region) and downwind (wake region) of wind farms. Nygaard [27] used the Jensen analytical wake model [28] to show that wind farm wakes can lead to considerable annual energy production losses in downwind neighboring wind farms. Bleeg et al. [29] used field measurements of multiple onshore wind farms to demonstrate that wind farms can induce velocity deficits upstream of the farms. However, few studies have focused on the whole flow field inside and around large finite size wind farms, including the induction and wake regions, and its adjustment to the fully-developed regime. Recently, Allaerts and Meyers [15,21] performed LESs of 15 km long wind farms with 20 wind turbine rows in CNBL flows to examine the effect of the inversion layer on wind-farm boundary layer flow and the induction of gravity waves. Despite the size of the wind farms simulated in those studies, the wind farm flows did not approach the fully-developed regime.

In this study, LES is used to simulate large finite-size wind farms in CNBL flows under different free-atmosphere thermal stratification strengths. The farm flow is investigated and compared to the no-farm and infinite wind farm flows. Special emphasis is placed on identifying and characterizing the key regions of the flow: induction, entrance and development, fully-developed, exit and farm-wake

regions. The effects of flow blockage produced by the wind farm and upwind propagating gravity waves (under subcritical flow conditions) on the induction and exit regions are quantified. The flow adjustment in the entrance and development region is studied and the distance required for the flow to reach its fully-developed region is investigated. The wake of the wind farms is also examined to provide insight into the wake recovery and its impact on neighboring wind farms. The rest of the manuscript is structured as follows: Section 2 introduces the LES framework and numerical setup, Section 3 describes the suite of simulations performed, Section 4 presents the results obtained from the numerical simulations and Section 5 concludes and discusses the results of the study.

2. Large-Eddy Simulations

2.1. LES Governing Equations and Modeling

The following filtered conservation of mass, filtered Navier-Stokes, and filtered potential temperature transport equations are solved by LES:

$$\frac{\partial \tilde{u}_i}{\partial x_i} = 0\,, \tag{1}$$

$$\frac{\partial \tilde{u}_i}{\partial t} + \tilde{u}_j \frac{\partial \tilde{u}_i}{\partial x_j} = -\frac{\partial \tilde{p}^*}{\partial x_i} - \frac{\partial \tau_{ij}^d}{\partial x_j} + \delta_{i3} g \frac{\tilde{\theta} - \langle \tilde{\theta} \rangle}{\theta_0} - \frac{f_i}{\rho} + F_i\,, \tag{2}$$

$$\frac{\partial \tilde{\theta}}{\partial t} + \tilde{u}_j \frac{\partial \tilde{\theta}}{\partial x_j} = -\frac{\partial \tilde{q}_j}{\partial x_j}\,, \tag{3}$$

where the tilde (˜) is a spatial filtering at scale $\tilde{\Delta}$, $\tilde{u}_i$ is the filtered velocity in the i-direction, $\tilde{\theta}$ is the filtered potential temperature, θ_0 is the reference temperature and the angle brackets ($\langle\,\rangle$) is a horizontal average over a specified area. τ_{ij}^d is the deviatoric part of the subgrid-scale (SGS) stress tensor ($\tau_{ij} = \widetilde{u_i u_j} - \tilde{u}_i \tilde{u}_j$), and $q_j = \widetilde{u_j \theta} - \tilde{u}_j \tilde{\theta}$ is the SGS heat flux vector. δ_{ij} is the Kronecker delta tensor, g is the gravitational acceleration, and ρ is the air density. $\tilde{p}^*$ is the modified pressure, and τ_{kk} is the isotropic part of the SGS stress tensor. f_i is a body force (per unit volume of air) used to model the effect of wind turbine induced forces on the flow, and F_i is the geostrophic forcing term. As the ABL flow is driven by an imposed uniform geostrophic wind with the effect of Coriolis, the forcing term is defined as: $F_i = f_c \epsilon_{ij3} (\tilde{u}_j - G_j)$, where f_c is the Coriolis parameter, ϵ_{ij3} is the Levi-Civita symbol, and G is the geostrophic wind. In this study, the Lagrangian scale-dependent dynamic model is used to parametrized the SGS turbulent fluxes [30–32].

The rotational actuator-disk model is used to parametrize the wind turbine induced forces f_i in Equation (2) [11–14,33]. The model accounts for the effects of non-uniform force distribution and turbine-induced flow rotation. In this model, wind turbine blades are comprised of N radial blade elements. The lift and drag forces acting on each blade element are parameterized based on the relative velocity, the geometry of the blade airfoil and the tabulated airfoil lift and drag coefficients. In this study, Vestas V-80 2 MW wind turbines with a diameter of $D = 80$ m and a hub height of $z_h = 70$ m are employed. Details on the rotational actuator-disk model and the turbine aerodynamic characteristics (e.g., the blade geometry, and the lift and drag coefficients) are provided by Wu and Porté-Agel [14].

2.2. Numerical Setup

The in-house WiRE LES code is used to simulate the interaction between large finite-size wind farms and the CNBL. The code is a modified version of the one introduced in [30,32–34], and it was described and used by Abkar and Porté-Agel [7,10] to simulate CNBL flow with different free-atmosphere stratification strengths in very large wind farms. A three-dimensional structured mesh is used, and the computational domain is discretized into N_x, N_y and N_z evenly spaced grid points in the streamwise, spanwise and vertical directions, respectively. The grid resolution of the domain is $\Delta x \times \Delta y \times \Delta z$. The mesh is staggered in the vertical direction, in which the lowest vertical

velocity component is located on the wall surface, and the lowest plane of other variables such as horizontal velocity, pressure and potential temperature are stored $\Delta z/2$ away from the surface. The vertical derivatives are approximated with a second-order finite-difference scheme, and the horizontal directions are treated with pseudospectral differentiation. The 3/2 rule [35] is used in the nonlinear term to eliminate the aliasing error. The LES equations are temporally advanced using the second-order Adams-Bashforth method [36].

The boundary conditions in the horizontal directions are periodic because of the pseudospectral differentiation scheme. A stress-free boundary condition is assigned to the top boundary with a Rayleigh damping layer similar to that used in [4,37] to avoid gravity wave reflection from the domain top. The temperature gradient at the top boundary is fixed at a constant prescribed lapse rate Γ (vertical gradient of the potential temperature). The instantaneous filtered shear stress at the bottom boundary is calculated using the standard formulation based on the application of Monin-Obukhov similarity theory for neutral boundary layers (i.e., the log law under neutral conditions) as follows [38,39]:

$$\tau_{i3}|_w = -u_*^2 \frac{\tilde{u}_i}{\tilde{u}_r} = -\left(\frac{\tilde{u}_r \kappa}{\ln(\frac{z}{z_o})}\right)^2 \frac{\tilde{u}_i}{\tilde{u}_r}, \tag{4}$$

where $\tau_{i3}|_w$ is the instantaneous wall stress, u_* is the friction velocity, z_o is the surface roughness, κ is the von Kármán constant, and $\tilde{u}_r$ is the local filtered horizontal velocity at the lowest level $(z = \Delta z/2)$. The surface heat flux is set to be zero since we are simulating CNBLs.

3. Suite of Simulations

To understand the interactions between the ABL and large finite-size wind farms, and the flow adjustment within the farms, a suite of LESs are performed for no-farm, large finite-size wind farm, and infinite wind farm cases. The primary set of LESs simulates CNBL flow across a large finite-size wind farm. The other two sets of simulations, no-farm cases and infinite wind farm cases, act as control simulations. The no-farm cases correspond to CNBL flows without wind farm. The second set of control simulations has wind farms occupying the entire computational domain and, therefore, represents an infinite wind farms due to the periodic boundary conditions in the horizontal directions. The flows in the no-farm cases and the infinite wind farm cases can be considered as the equilibrium flows upwind and downwind of the simulated large finite-size wind farm, had the farm been long enough to approach its asymptotic infinite wind farm regime.

In all of the simulations, the CNBL flow is driven by a geostrophic wind of $G = 10$ m·s^{-1}, and the Coriolis parameter is set to $f_c = 1.195 \times 10^{-4}$ rad·s^{-1} (i.e., equivalent to the latitude of the North Sea). The surface roughness is set to $z_o = 0.05$ m and the reference potential temperature is $\theta_0 = 293$ K. The value of these parameters is set such that the inflow conditions generated for the wind farm simulations are comparable to those in the North Sea [40]. The simulations are initialized with a constant velocity in the streamwise direction of 10 m·s^{-1}. The potential temperature is initialized with a prescribed constant temperature lapse rate Γ. Very small random perturbations are added to the velocity and the temperature fields at the lowest 100 m to induce the development of turbulence. The wind farms simulated are in both aligned and staggered configurations with a streamwise turbine spacing (s_x) and a spanwise turbine spacing (s_y) of 7 D. The simulations of the no-farm and the infinite wind farm cases are run for 8 h, while the simulations of the large finite-size wind farm cases are run for 6 h. The statistics presented in the latter sections are averaged over the last hour of the simulations, when quasi-steady flow conditions are guaranteed. Table 1 summarizes the key parameters of the various simulations carried out in this study.

Table 1. Suite of LES Simulations.

Case	Γ (K/km)	Number of Turbines	$s_x \times s_y$	Turbine Arrangement	$L_x \times L_y \times L_z$ (km^3)	$N_x \times N_y \times N_z$
No-Farm Case						
NF-Γ1	1	-	-	-	$14 \times 2.8 \times 2.4$	$350 \times 175 \times 240$
NF-Γ5	5	-	-	-	$14 \times 2.8 \times 2.4$	$350 \times 175 \times 240$
Large Finite-Size Wind Farm Case						
FS-sΓ1	1	36×5	$7D \times 7D$	Staggered	$42 \times 2.8 \times 2.4$	$1050 \times 175 \times 240$
FS-aΓ1	1	36×5	$7D \times 7D$	Aligned	$42 \times 2.8 \times 2.4$	$1050 \times 175 \times 240$
FS-sΓ5	5	36×5	$7D \times 7D$	Staggered	$42 \times 2.8 \times 2.4$	$1050 \times 175 \times 240$
FS-aΓ5	5	36×5	$7D \times 7D$	Aligned	$42 \times 2.8 \times 2.4$	$1050 \times 175 \times 240$
Infinite Wind Farm Case						
Inf-sΓ1	1	8×4	$7D \times 7D$	Staggered	$4.5 \times 2.8 \times 2.4$	$112 \times 140 \times 240$
Inf-aΓ1	1	8×4	$7D \times 7D$	Aligned	$4.5 \times 2.8 \times 2.4$	$112 \times 140 \times 240$
Inf-sΓ5	5	8×4	$7D \times 7D$	Staggered	$4.5 \times 2.8 \times 2.4$	$112 \times 140 \times 240$
Inf-aΓ5	5	8×4	$7D \times 7D$	Aligned	$4.5 \times 2.8 \times 2.4$	$112 \times 140 \times 240$

3.1. No-Farm Case

As shown in Figure 1, the ABL flow without wind farm is characterized by a mean hub-height velocity of 8 m·s^{-1} and a turbulence intensity (TI) of 7% for $\Gamma = 1$ K. The hub height velocity is 7.8 m·s^{-1} and the turbulence intensity (TI) is 6.5% for $\Gamma = 5$ K. The turbulence intensity is calculated as:

$$TI = \frac{\sqrt{\frac{2}{3}k}}{\overline{M}_{hub}}, \tag{5}$$

where k is the turbulence kinetic energy (TKE), $\overline{M}_{hub}$ is the mean velocity magnitude at hub height (the overbar indicates temporal averaging). These flow characteristics agree well with the measured inflow data at the Horns Rev wind farm [40].

3.2. Large Finite-Size Wind Farm Simulations

A precursor simulation technique, which was used successfully in previous finite wind farm studies [11,14,17,20,41], is adopted for the large finite-size wind farm simulations. The precursor simulations without wind farm are run until the ABL flow reaches quasi-steady state, similar to the no-farm cases, with the computational domain size of the large finite-size wind farm simulations. However, as the Coriolis force in the governing Navier-Stokes equations (Equation (2)) changes the flow direction inside the ABL with height, a wind direction control algorithm similar to the ones used in [20,42] is implemented to ensure the inflow conditions for the wind farm simulations align with the first wind turbine row. In the algorithm, a source term is added to the governing momentum equations to adjust the geostrophic wind gradually. After reaching quasi-steady flow conditions, the simulations are run for another 6 h, during which the instantaneous velocity and potential temperature fields are saved and later imposed as the inflow fields for the large finite-size wind farm simulations. To adjust the flow from the far-wake flow to the inflow obtained from the precursor simulations, a buffer zone is applied downwind of the wind farm. Figure 2 summarizes the size of the computational domain and illustrates the layout of the simulated large finite-size wind farms.

3.3. Infinite Wind Farm Simulations

Simulations of ABL flow without a wind farm are performed again using the specified computational domain for the infinite wind farm simulations. The simulated ABL flows are then fed into the infinite wind farm simulations as initial conditions.

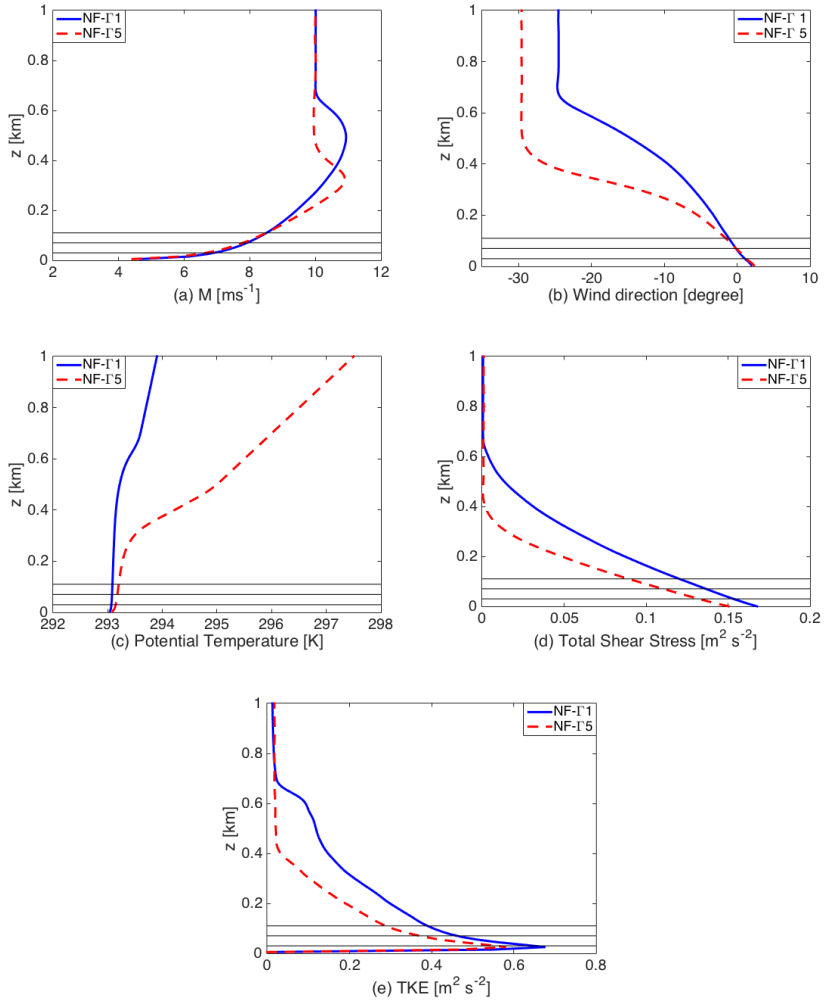

Figure 1. Vertical profiles of the horizontally-averaged ABL flow characteristics in the no-farm cases: (**a**) mean velocity magnitude $\overline{M}$; (**b**) wind direction; (**c**) potential temperature; (**d**) total Reynolds shear stress $((\overline{u'w'})^2 + (\overline{v'w'})^2)^{1/2}$; and (**e**) TKE. The black solid lines represent the top-tip, hub, and bottom-tip heights.

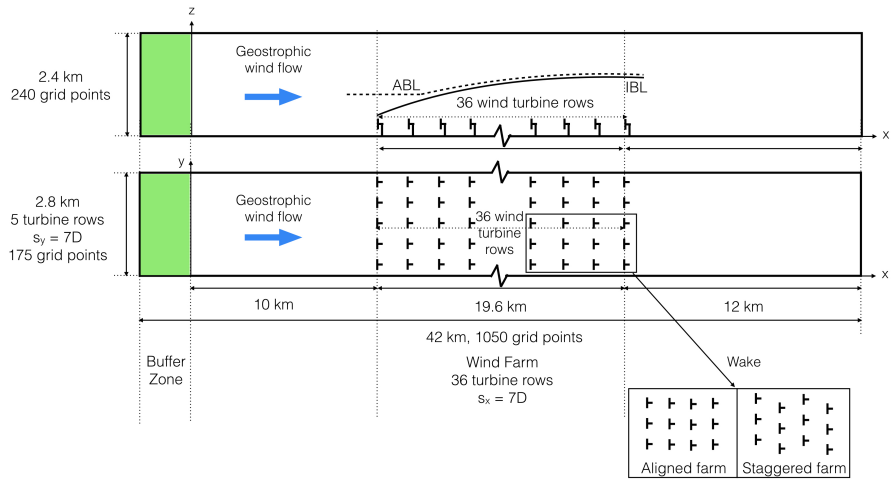

Figure 2. Computational domain and layout of the large finite-size wind farms simulated.

4. Results

In this section, the adjustment of the simulated flow inside and around the large wind farms is studied for the different cases resulting from the combination of the two farm layouts (aligned and staggered) and free-atmosphere stratification strengths ($\Gamma = 1$ K/km and 5 K/km) considered in this study. The results will be presented and discussed for the different flow regions that have been identified in the course of this research. The identified flow regions are:

(i) The induction region, immediately upwind of the wind farm, where flow deceleration is induced by the wind farm due to the cumulated wind turbine blockage effect. If free-atmosphere stratification is strong enough, it could lead to a gravity-wave-induced blockage effect triggered by the farm. As a result, in that case, the velocity in this region would be significantly reduced, and the induction region could extend a few kilometers upwind of the farm.

(ii) The entrance and development region, extending immediately downwind of the leading edge of the wind farm, where the flow is decelerated because of the momentum extraction by the wind turbines. The deceleration results in an upward mass flux from the wind farm top, which slows down the flow above the farm and causes an internal boundary layer (IBL) growth. For wind farms that are large enough, the IBL could reach the ABL height and result in a modification of the ABL depth.

(iii) The fully-developed region, following the entrance and development region, in which changes of flow characteristics in the streamwise direction are negligible throughout the ABL, and thus the flow is considered to be fully developed. In this region, both the IBL and ABL depths are constant and equal to the height of the infinite wind farm ABL.

(iv) The exit region, upwind of the trailing edge of the wind farm, where the flow accelerates and a downward mass flux is present, resulting in a decrease in the IBL and ABL heights. If free-atmosphere stratification is strong, the downward flow could trigger upwind propagating gravity waves and an advantageous pressure gradient at the trailing farm edge. As a consequence, in that case, the favorable gravity-wave-induced pressure gradient would lead to a substantial flow acceleration in the region. The exit region could extend a few kilometers upwind of the end of the farm, similar to the length of the induction region.

(v) The wind farm wake region, downwind of the wind farm trailing edge, in which the flow recovers and returns to its undisturbed inflow velocity profile.

Belcher et al. [43] proposed similar flow adjustment regions for canopy flows, although they did not consider the interaction between the IBL and ABL. Figure 3a shows the schematic of the different flow regions for a large finite-size wind farm under weak free-atmosphere stratification, in which the induction region is small, and the exit region is not present. Figure 3b displays the flow regions of a farm under strong free-atmosphere stratification, in which all regions are present.

4.1. Wind Farm Induction Region

Contour plots of the time-averaged velocity magnitude through the center of a wind turbine column are shown in Figure 4. The ABL depth (i.e., the white lines in Figure 4) is traced and defined as the lowest height at which the time- and spanwise-averaged velocity magnitude equals the geostrophic velocity magnitude [7]. The ABL height for the corresponding no-farm and infinite wind farm cases is also shown in Figure 4 for comparison. It is worth mentioning that the infinite wind farm ABL heights obtained from the LES results agree well with those predicted by the expression proposed by Abkar and Porté-Agel [7]:

$$\delta_{bl} = C_R(1 + C_N \frac{N}{|f_c|})^{-\frac{1}{2}} \frac{u_{*2}}{f_c} + z_h + \frac{D}{2}, \quad (6)$$

where $C_R = 0.16$ and $C_N = 0.035$ are empirical dimensionless constants, $N = \sqrt{\frac{g}{\theta_0}\Gamma}$ is the Brunt-Väisälä (buoyancy) frequency of the upper stably stratified free atmosphere, and u_{*2} is the friction velocity at the turbine top-tip level.

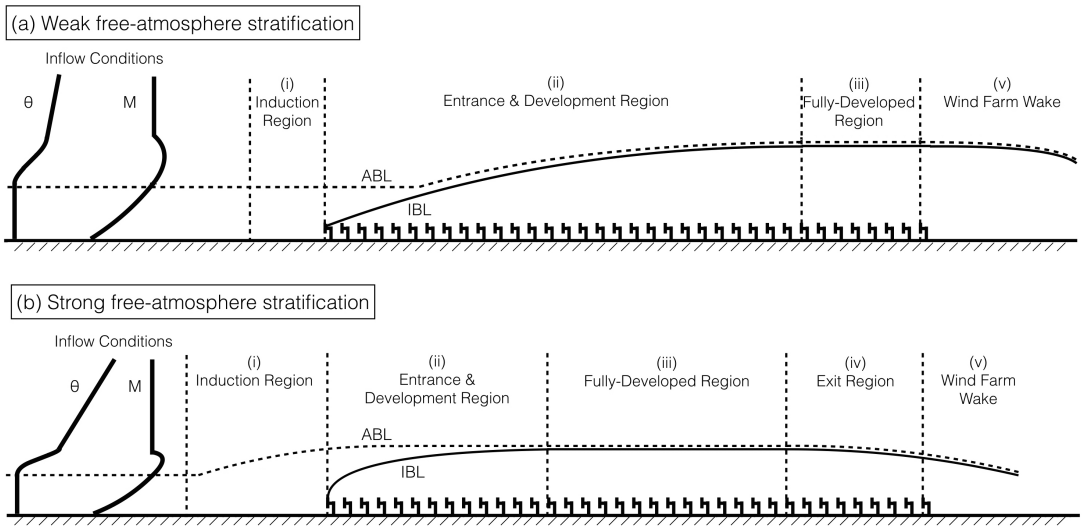

Figure 3. Flow adjustment regions in large finite-size wind farms in CNBLs with (**a**) weak and (**b**) strong free-atmosphere stratification. The flow can be divided into the following regions: (i) induction region; (ii) entrance and development region; (iii) fully-developed region; (iv) exit region; (v) wind farm wake.

As a wind turbine extracts momentum from the inflow, it produces a local turbine blockage effect, which leads to a velocity lower than the one of the inflow immediately upstream of the turbine, in the so-called turbine induction zone [44,45]. The flow velocity upwind of a wind farm is expected to further reduce because of the cumulated turbine blockage effect [46]. A recent study by Bleeg et al. [29] showed that the velocity deficit upstream of a farm caused by the wind farm blockage could be as high as 3% 2.5 D upstream of the wind farm based on wind mast measurements from multiple onshore wind farms. For the wind farms simulated in this study, under $\Gamma = 1$ K/km, the induction region is less than 1 km as shown in Figure 5. A 1.2% velocity deficit is observed 2.5 D upstream of the first turbine row for the aligned and staggered cases, similar to the value reported by Branlard [46]. The velocity deceleration in the induction region is more significant under $\Gamma = 5$ K/km than that under $\Gamma = 1$ K/km. The induction region extends up to 7 km, and a 10% and 11% velocity deficit is observed for the aligned and staggered farm cases, respectively, under the strong stratification.

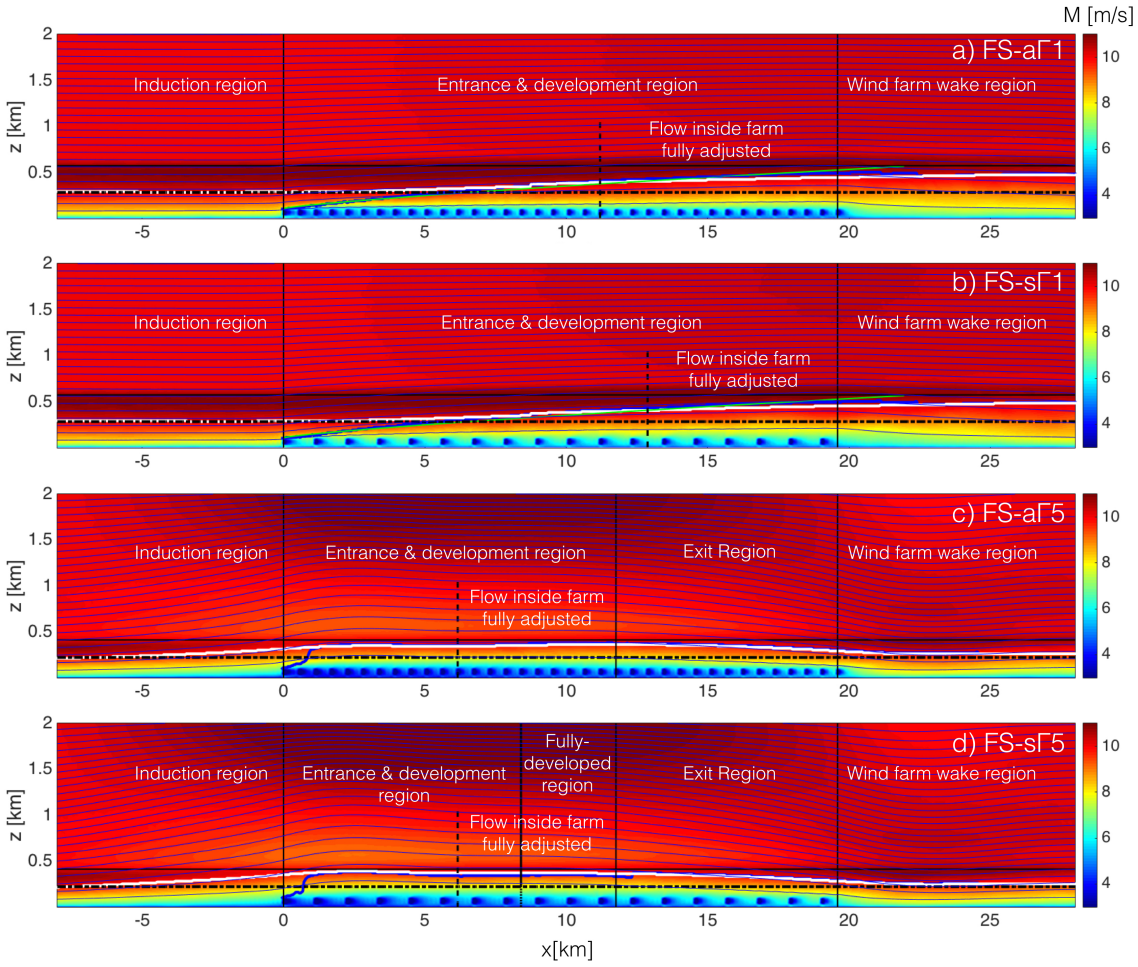

Figure 4. Contours of time-averaged horizontal velocity magnitude M on the xz plane through the center of a wind turbine column for the case (**a**) FS-aΓ1; (**b**) FS-sΓ1; (**c**) FS-aΓ5; (**d**) FS-sΓ5. The IBL height (thick blue line), the CNBL height (white line), the CNBL height of the inflow (dashed black line), Elliot's 0.8 power law (bright green line) and the CNBL height with an infinite wind farm (solid black line) are also included. The thin blue lines are the velocity streamlines (i.e., the vertical component is made larger by a scale factor of 5). The black vertical solid lines indicate the start and end of different flow regions.

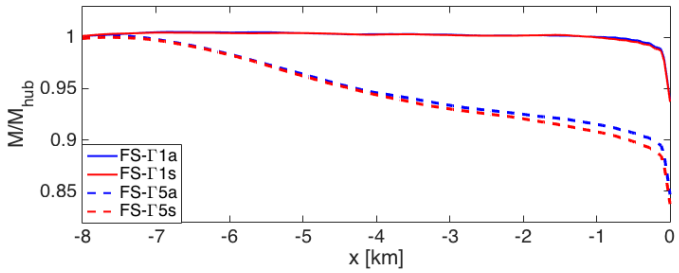

Figure 5. Time- and spanwise-averaged velocity magnitude at the hub height in the wind farm induction region, normalized by the inflow velocity magnitude at hub height.

The large extent of the induction region and the low velocity induced upstream of the farm in the $\Gamma = 5$ K/km cases can be explained by the gravity-wave-induced blockage effect triggered by the large finite-size wind farms under strongly stratified free atmosphere. These gravity waves are commonly observed in flow over mountains [47,48]. Smith [49] used a linear quasi-analytical

model to suggest that gravity waves can be induced by large finite-size wind farms. Allaerts and Meyers [15,21] showed that the upward displacement of the boundary layer by flow deceleration in the wind farm excites gravity waves, supporting the suggestion from Smith [49]. Reinecke and Durran [50], and Vosper et al. [51] demonstrated that a Froude number could be used to characterize the blocking behavior of flow over mountains and the onset of upwind mountain stagnation. Using a similar approach, the Froude number:

$$Fr = \frac{U}{\sqrt{g' z_i}}, \tag{7}$$

is estimated here to characterize the simulated flows under $\Gamma = 1$ K/km and $\Gamma = 5$ K/km. In Equation (7), U is the boundary-layer bulk velocity, $g' = g\frac{\theta(D_h)-\theta_0}{\theta_0}$ is the reduced gravity taking into account the stability variation between the ground and a depth scale D_h, and z_i is the height above which the stability is independent of height and is prescribed with a fixed Γ. Vosper et al. [51] demonstrated that the thermal stability over a mountain has a significant effect on the gravity-wave-induced flow blockage, and the depth scale $D_h = z_i + \frac{U}{N}$ could account for such stability effect on mountain flows. The Fr of a flow is the ratio of the flow speed to the speed of the induced gravity waves. When $Fr < 1$, the flow is subcritical and, therefore, any gravity waves induced by vertical flow displacement (e.g., due to the the presence of a hill or a wind farm) will propagate upwind. In contrast, for $Fr > 1$, the flow is supercritical and gravity waves cannot propagate upwind. Under $\Gamma = 5$ K/km, using Equation (7) yields $Fr = 0.94$, showing that the flow is subcritical and thus, prompt to the triggering of upwind propagating gravity waves. In contrast, under $\Gamma = 1$ K km, $Fr = 1.31$, which indicates that the flow is supercritical and no upwind propagating gravity waves can be triggered. The values of above-mentioned variables related to the calculation of Fr are presented in Table 2 for both thermal stability cases.

Table 2. The values of U, z_i, D_h, $\theta(D_h)$, N and Fr.

Γ (K/km)	U (m·s^{-1})	z_i (m)	N (s^{-1})	D_h (m)	$\theta(D_h)$ (K)	Fr
$\Gamma = 1$	9.63	710	0.0057	2370	295	0.94
$\Gamma = 5$	8.05	510	0.013	1220	299	1.31

As the flow approaches the leading edge of the wind farms, there is an upward displacement of the low-velocity flow (shown by the streamlines in Figure 4) caused by vertical momentum advection. The upward movement of the flow leads to an upward displacement of the capping stable layer, also often loosely referred to as the capping inversion, at the entrance of the farms under $\Gamma = 5$ K/km, as shown in Figure 6b. The upward displacement of the flow triggers gravity waves and associated pressure disturbances. As the flow is subcritical in the cases under $\Gamma = 5$ K/km, the gravity waves and the pressure disturbances induced propagate upwind of the wind farm, generating a high-pressure region at the leading edge, which extends far upstream of the wind farms, as shown in Figure 6d. As a result, there exists a gravity-wave-induced blockage effect triggered by the wind farm, similar to the mountain blockage effect in subcritical flows over mountains, which decelerates the flow upwind of the farm significantly. In contrast, as the flow is supercritical in the cases under $\Gamma = 1$ K/km, gravity waves cannot propagate upwind, and thus there is no gravity-wave-induced blockage effect triggered by the farm. As a result, the deceleration is less significant in the induction region as it is only caused by the cumulative turbine blockage effect.

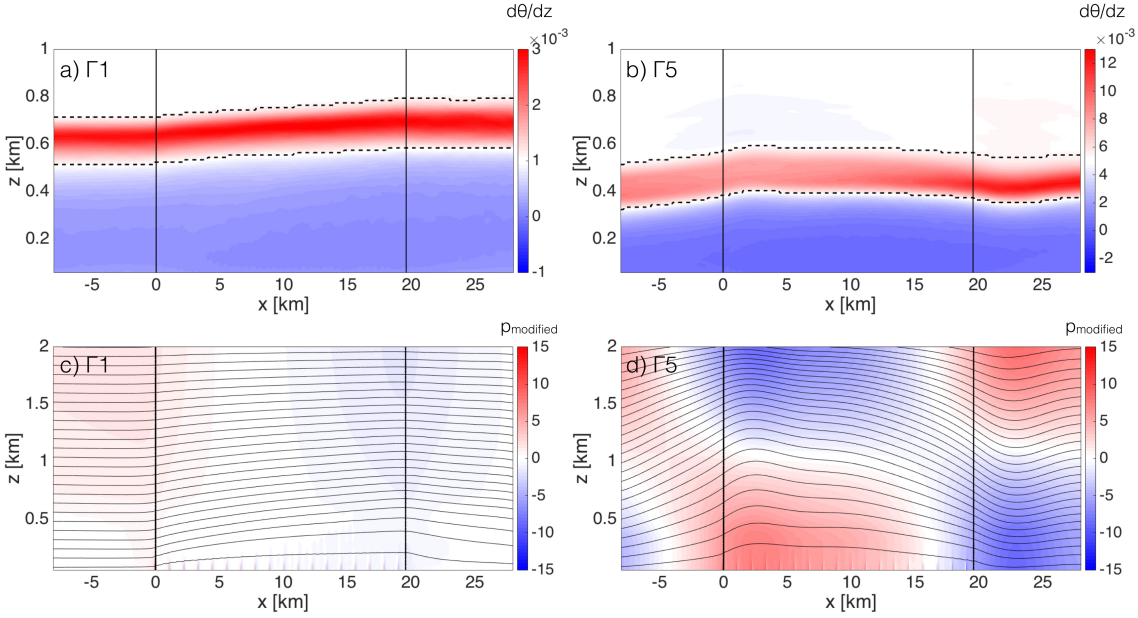

Figure 6. Contours of time- and spanwise-averaged vertical potential temperature gradient $d\theta/dz$ for the case (**a**) FS-sΓ1; (**b**) FS-sΓ5. The dotted black lines indicate the bottom and the top heights of the capping inversion. Contours of time- and spanwise-averaged modified pressure for the case (**c**) FS-sΓ1; (**d**) FS-sΓ5. The vertical solid black lines indicate the streamwise positions of the beginning and the end of the wind farm. Results are not shown for the aligned farms as they are similar to the staggered farms.

4.2. Wind Farm Flow Entrance and Development Region

4.2.1. Velocity Adjustment

In this section, vertical profiles of the time- and spanwise-averaged velocity magnitude at different wind turbine rows, shown in Figure 7 together with the corresponding inflow and infinite wind farm profiles, are examined to characterize the flow inside and above the large finite-size wind farms. We consider the mean flow inside the wind farm as fully adjusted when the change of the vertical profile of velocity magnitude at a particular wind turbine row is less than 1% of the previous turbine row profile. The overall mean flow of the wind farm is considered to be fully developed when the flow is within 1% threshold of the corresponding infinite wind farm velocity magnitude throughout the ABL height.

Under $\Gamma = 1$ K/km, the flow in both farms gradually decelerates as it enters the wind farm. The mean flow inside the farm is fully adjusted at the 21th turbine row for the aligned case and the 24th row for the staggered case, which agrees with the faster velocity adjustment observed in aligned farms compared with staggered farms by Wu and Porté-Agel [13]. However, the mean flow above both farms deviates does not reach its fully-developed regime.

Under $\Gamma = 5$ K/km, the flow in both farms shows a different adjustment trend from that under $\Gamma = 1$ K/km. Due to the significant flow deceleration in the induction region caused by the gravity-wave-induced blockage effect, the flow velocity is much lower at the wind farm entrance under $\Gamma = 5$ K/km than under $\Gamma = 1$ K/km. As the flow enters the wind farm (i.e., entrance and development region), the flow inside the turbine rotor region decelerates due to the extraction of momentum by the wind turbines. The flow inside the farm reaches its minimum velocity magnitude at the 5th row, then reaccelerates from the 5th row to the 11th row. Such flow reacceleration behavior in the entrance and development region is also observed in low flow-blockage shallow canopy flows by Rominger and Nepf [52]. The flow inside the farm continues to develop and becomes fully adjusted from the 12th row to the 21st row. The overall mean flow of the staggered farm under $\Gamma = 5$ K/km

becomes fully-developed from the 16th row to the 21th row, showing that the flow inside the farm adjusts faster than the flow above the farm. As the flow inside the farm approaches the wind farm exit region, the flow begins to accelerate at the 22nd row, a location significantly upstream of the trailing edge of the wind farm. Towards the trailing edge of the wind farm, there is a strong downward movement of the subcritical flow, as shown in Figure 4d. As a result, the capping inversion displaces downward and restores to its original depth, as seen in Figure 6b. The downward movement of the capping inversion triggers gravity waves and generate a low-pressure region at the wind farm trailing edge (shown in Figure 6d), in contrast to the high-pressure region at the wind farm entrance. The gravity waves and favorable pressure gradient induced at the wind farm end propagate upwind, thus promoting a downward accelerating flow that extends upwind 7 km in the so-called wind-farm exit region. The length of the exit region is similar to the length of the induction region.

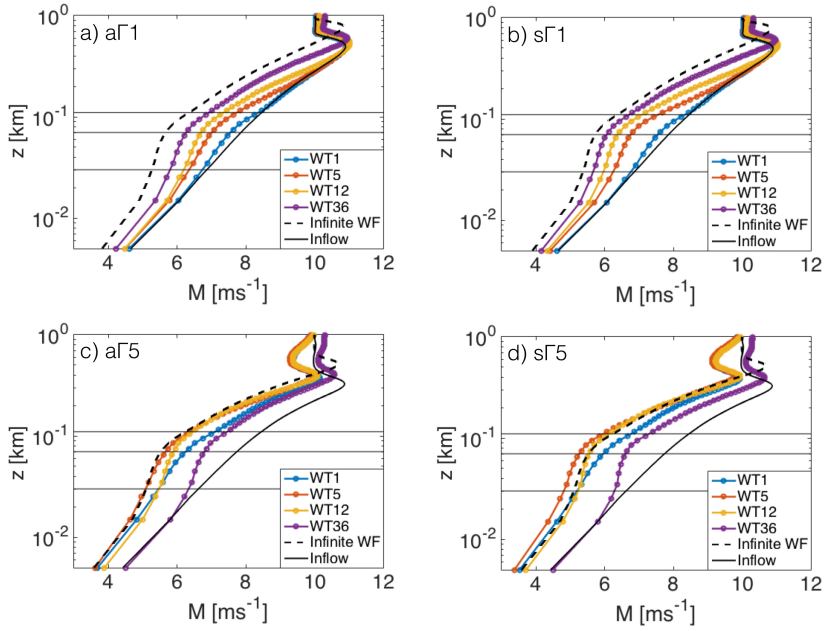

Figure 7. Vertical profiles of time- and spanwise-averaged velocity magnitude at the 1st, 5th, 12th and 36th turbine rows for the cases: (**a**) FS-aΓ1; (**b**) FS-sΓ1; (**c**) FS-aΓ5; and (**d**) FS-sΓ5. The black solid profile represents the velocity magnitude of the ABL inflow, and the black dashed profile represents the time- and horizontal-averaged velocity magnitude of the infinite wind farm with the same wind farm configuration. The black horizontal solid lines represent the turbine top-tip, hub and bottom-tip heights.

The flow inside the aligned farm under $\Gamma = 5$ K/km shows a similar adjustment trend as the staggered farm flow under $\Gamma = 5$ K/km. It decelerates to its minimum at the 5th row, reaccelerates in the entrance and development region and becomes fully adjusted from the 12th row until the 21st row. However, the flow above the farm does not reach its fully-developed wind farm regime, which can be attributed to the presence of high-speed channels between turbine columns throughout the aligned farm, similar to the results shown by Wu and Porté-Agel [13]. These channels increase the heterogeneity of the flow above the farm, which needs larger distances to adjust and reach the fully-developed regime. The flow accelerates from the 22nd row as it reaches the exit region. Figure 8 shows the hub height velocity magnitude at each turbine row for all the wind farm cases to demonstrate the overall velocity adjustment trend discussed. Overall, the mean velocity shows a larger decrease in the staggered farm case than the aligned one, similar to the results shown by Wu and Porté-Agel [13].

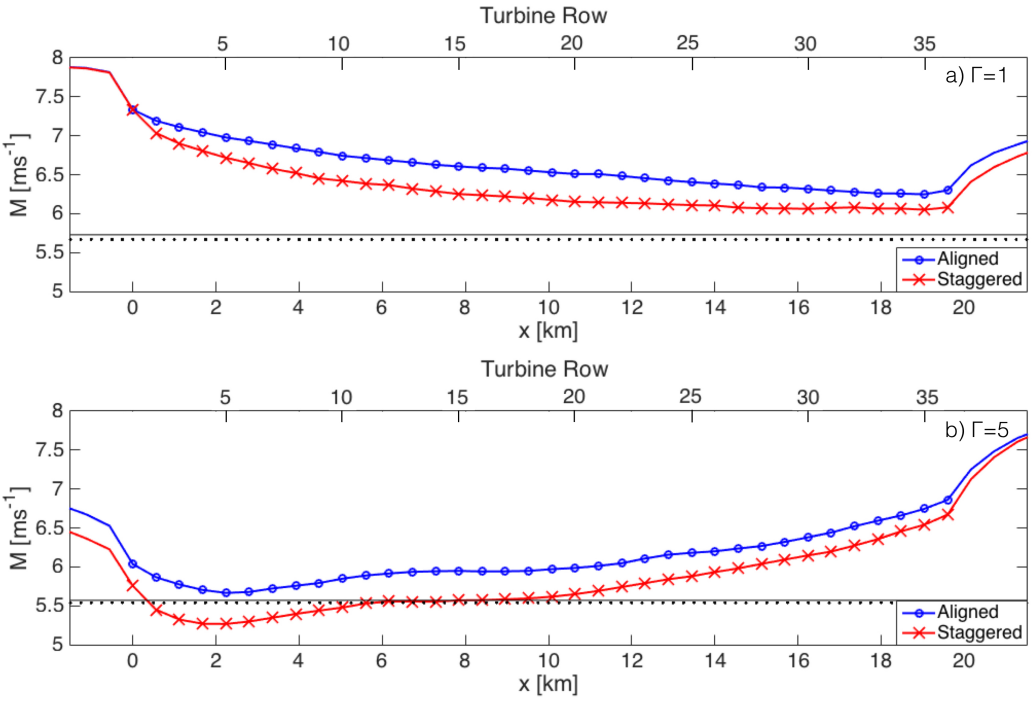

Figure 8. Time- and horizontally-averaged (the distance of streamwise averaging is 7D, with the turbine row placed at the center) velocity magnitude at the hub height at different wind turbine rows for the wind farm cases under (**a**) $\Gamma = 1$ K/km; and (**b**) $\Gamma = 5$ K/km. The black horizontal dotted and solid lines are the time- and horizontally-averaged velocity magnitude at the hub height for the corresponding aligned and staggered infinite wind farm cases, respectively

4.2.2. IBL and ABL Growth

Next, the growths of the IBL and the ABL are investigated for all the farm cases, and their depths are compared against the corresponding infinite wind farm cases. The deceleration inside the entrance and development region results in an upward mass flux at the top of the wind farm caused by vertical momentum advection [53,54]. The upward displacement of the low-velocity flow from the rotor region decelerates the flow above the wind farm entrance and development region, leading to an IBL. The IBL height (i.e., the blue lines in Figure 4) is identified as the lowest level above the wind farm at which the time- and spanwise-averaged horizontal velocity magnitude lies within 3% of the mean inflow velocity at the same level 1 km upstream of the wind farm [13,21,55].

Under $\Gamma = 1$ K/km, the IBL grows gradually as the flow enters the wind farm. At the 12th turbine row, the IBL interacts with the thermally-stratified free atmosphere above and modifies the ABL height, while the stratified free-atmosphere suppresses the IBL growth. Beyond this point, the IBL and ABL grow together at a steady rate. Elliot [56] showed that IBLs developing downwind of a smooth-to-rough transition grow with downwind distance according to a 0.8 power law and can be predicted by the following empirical formula:

$$\frac{\delta}{z_{02}} = (0.75 - 0.03)\ln(\frac{z_{02}}{z_{01}})(\frac{x}{z_{02}})^{0.8}, \quad (8)$$

where z_{01} and z_{02} are the surface roughness upwind and downwind, and x is the distance measured from the roughness change. The IBL growth over the wind farms under $\Gamma = 1$ K/km is approximated using Elliot's 0.8 power law (i.e., the green lines in Figure 4a,b). The upwind surface roughness is $z_{01} = 0.05$ m, and the downwind surface roughness is $z_{02} = 1.07$ m. The downwind surface roughness is obtained by using the wind farm effective roughness equation proposed by Abkar and Porté-Agel [7], which takes the CNBL conditions into account. It is shown that the IBL height obtained from the

LES results for the $\Gamma = 1$ K/km cases is similar to the IBL height approximated by Elliot's 0.8 power law using the wind farm effective roughness as the downwind surface roughness. However, the IBL growth deviates from the 0.8 power law at the 30th turbine row as the IBL and ABL continue to approach the infinite wind farm ABL height. The IBL and ABL do not grow to the infinite wind farm ABL height even at the trailing edge of the wind farm for the $\Gamma = 1$ K/km cases, indicating the flow above the farm is not fully developed since the mean flow velocity above the farm has not approached the infinite wind farm regime as discussed in the previous section.

The IBL and ABL growth trends are different for the cases under $\Gamma = 5$ K/km. A fast IBL growth is observed under strong stratification. For the staggered case under $\Gamma = 5$ K/km, inside the entrance and development region, the IBL reaches the ABL at the second turbine row. Moreover, both the IBL and ABL grow to the infinite wind farm ABL height at the 5th turbine row, where the flow inside the farm reaches its minimum velocity magnitude. The abrupt IBL growth at the farm entrance is due to the strong upward displacement of the low-velocity flow above the farm leading edge and the gravity-wave-induced blockage effect which decelerates the flow and deflects it upwards upstream of the wind farm as mentioned in Section 4.1. The IBL and ABL heights then remain almost constant from the 5th row until the 21st row. Both the IBL and the ABL heights in the fully-developed region correspond to the infinite wind farm ABL height. The IBL and ABL heights start to decrease at the 22th turbine row as the flow approaches the exit region of the wind farm and starts to accelerate. A similar trend is observed for the IBL and ABL growth of the aligned farm under $\Gamma = 5$ K/km.

4.2.3. Turbulent Shear Stress Adjustment

To further examine the flow adjustment inside large finite-size wind farms, the vertical profiles of time- and spanwise-averaged total turbulent (Reynolds) shear stress on the horizontal plane (i.e., $((\overline{u'w'})^2 + (\overline{v'w'})^2)^{1/2}$) at various turbine rows for the different wind farm cases are shown in Figure 9. In general, the total shear stress throughout the ABL is higher under the weaker free-atmosphere stratification, demonstrating that downward flow entrainment into the wind farm increases for lower free-atmosphere stability [7]. Due to the strong wind shear at the turbine top tip, the total shear stress peaks at the top-tip level of the turbines throughout the whole wind farm. Inside the entrance and development region, the shear stress experiences a rapid growth between the second and third turbine rows, followed by a reduced growth rate at the latter turbine rows in all the wind farm cases. This delay of shear stress adjustment is likely due to the flow distortion at the entrance edge of the wind farm, similar to the trend observed across a forest edge by Morse et al. [57].

The total shear stress at the turbine top-tip level reaches its equilibrium value at the 10th and 8th turbine rows for the aligned and staggered farm cases, respectively, under $\Gamma = 1$ K/km, and at the 8th and 5th turbine rows under $\Gamma = 5$ K/km. It is shown that the shear stress adjusts faster under a stronger free-atmosphere stratification inside wind farms with the same farm configuration. A staggered farm configuration also promotes faster shear stress adjustment. Moreover, the shear stress adjusts faster than the mean flow velocity, as suggested by Shir [58] in flow over surface roughness transitions. For the case FS-sΓ5, the shear stress profile throughout the turbine height matches well with the profile from the infinite farm case inside the region where the mean flow inside the wind farm is fully adjusted (i.e., from the 12th turbine row to the 21st row). An upward propagation of the total shear stress is observed above the turbine top-tip level. As the flow approaches the exit region of the wind farm, an increase of shear stress is observed due to an increase of turbulent momentum exchange as the downward flow accelerates. The increase of the shear stress at the exit region is also observed in the aligned case under $\Gamma = 5$ K/km, yet it is lower than that in the staggered case.

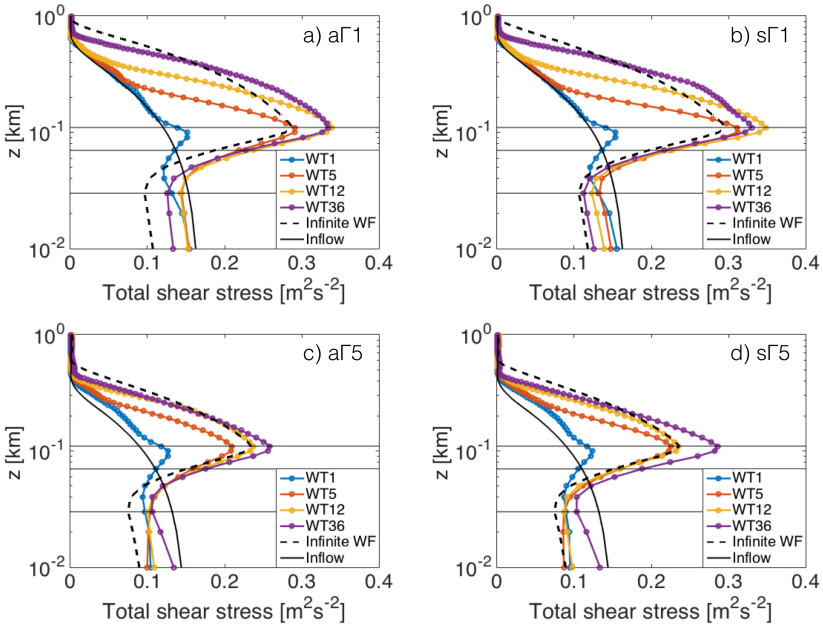

Figure 9. Vertical profiles of time- and spanwise-averaged total shear stress at the 1st, 5th, 12th and 36th turbine rows for the cases: (**a**) FS-aΓ1; (**b**) FS-sΓ1; (**c**) FS-aΓ5; and (**d**) FS-sΓ5. The black solid profile represents the total shear stress of the ABL inflow, and the black dashed profile represents the time- and horizontal-averaged total shear stress of the infinite wind farm with the same wind farm configuration. The black horizontal solid lines represents the top-tip, hub and bottom-tip heights.

4.2.4. TKE Adjustment

The adjustment of vertical profiles of time- and spanwise-averaged TKE inside the large finite-size wind farms is shown in Figure 10. The TKE peaks slightly below the turbine top tip level due to the strong wind shear and high Reynold stress at the top-tip level of the wind turbines. In all the cases considered, the TKE grows rapidly at the first two turbine rows. Under the same stratification, the aligned wind farm configuration leads to a higher TKE distribution throughout the whole farm than the staggered configuration. This is because, in the staggered configuration, there is a longer distance behind each turbine for the TKE to dissipate. Meanwhile, in the aligned configuration, the short distance between turbines limits the amount of turbulence dissipation as discussed in [13]. For the case FS-sΓ5, similar to the shear stress profile, the TKE profile throughout the turbine height matches well with the profile from the infinite farm case inside the region where the mean flow inside the wind farm is fully adjusted. From the 7th to the 21th turbine rows, the TKE profile above the wind farm continues to approach the infinite wind farm TKE profile. At the 22nd turbine row, where the flow reaches its exit region and starts to accelerate, the TKE profile within the rotor region increases and departs from the infinite wind farm profile. For the case FS-aΓ5, an increase in the TKE is also observed as the flow approaches the exit region. As the turbulent shear stress contributes to the production of TKE, the TKE adjustment shows a similar trend to that of the turbulent stress and it is faster than the mean flow velocity adjustment.

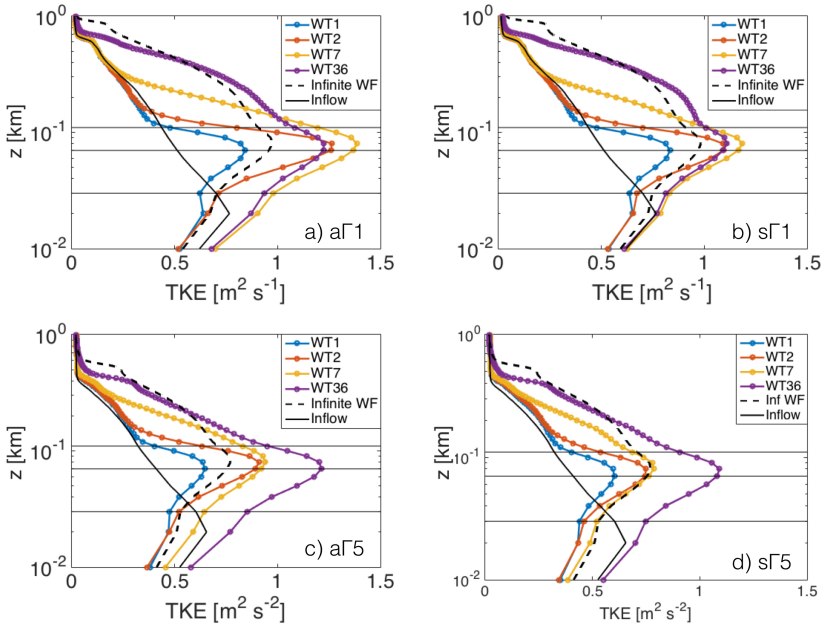

Figure 10. Vertical profiles of time- and spanwise-averaged TKE at the 1st, 2nd, 7th, and 36th turbine rows for the cases: (**a**) FS-aΓ1; (**b**) FS-sΓ1; (**c**) FS-aΓ5; and (**d**) FS-sΓ5. The black solid profile represents the TKE of the ABL inflow, and the black dashed profile represents the time- and horizontal-averaged TKE of the infinite wind farm with the same wind farm configuration. The black horizontal solid lines represents the top-tip, hub and bottom-tip heights.

4.2.5. Wind Farm Power Output

The wind farm power output averaged over a turbine row and normalized by the power output of a stand-alone wind turbine operating in the same ABL conditions is shown in Figure 11. Overall, the power output decreases significantly at the second row in all the aligned farm cases, in contrast to the gradual reduction in the staggered wind farm cases, as previously reported by Wu and Porté-Agel [13], and Stevens et al. [59]. The staggered wind farms generate more power than the aligned wind farms, agreeing with the results of Porté-Agel et al. [60]. Besides, the power production reduction at the first few turbine rows is more gradual in the staggered farms than that in the aligned farms as the flow in staggered wind farms has a longer distance to recover its velocity deficit between consecutive turbine rows comparing to aligned farms [13]. The staggered wind farm is thus more efficient in extracting momentum from the incoming flow.

The turbine power output normalized by the power output of a stand-alone turbine allows us to understand how the velocity deficit induced by the farms inside the induction region affects the wind farm performance. Under $\Gamma = 1$ K/km, the velocity deficit induced by the farms causes a 1.3% power deficit at the first turbine row in the aligned wind farm and a 3% power deficit in the staggered farm. Under $\Gamma = 5$ K/km, the power deficit at the first turbine row is as high as 35% and 41% for the aligned and staggered configurations, respectively, due to the high velocity deficit in the induction region caused by the gravity-wave-induced blockage effect. Since the wind farms simulated are infinite in the spanwise direction, the effect of the induction region shown is likely exaggerated comparing to that in the real farm cases. However, the significant power deficit at the first turbine row suggests that the induction region of wind farms cannot be neglected in future studies as it could impact the flow inside of the wind farm, especially at the first few turbine rows.

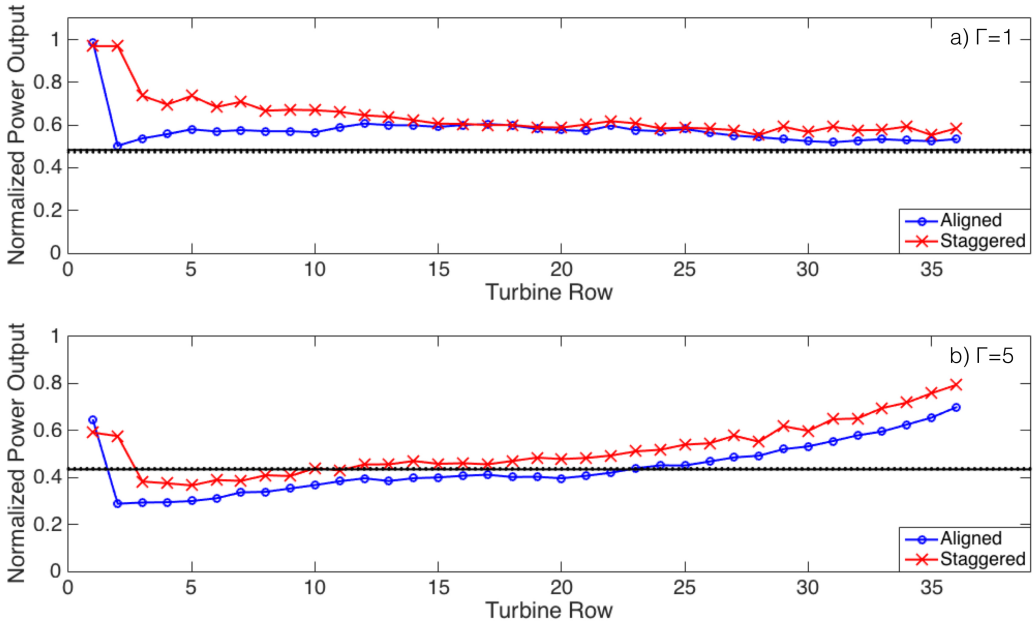

Figure 11. Power production at different turbine rows inside the wind farms for the (**a**) $\Gamma = 1$ K/km cases and (**b**) $\Gamma = 5$ K/km cases, normalized by the power production of a single turbine operating under the same lapse rate. The black horizontal dotted and solid lines are the power production of a wind turbine for the corresponding aligned and staggered infinite wind farm cases, respectively.

Dissimilarities are observed in the power output under different free-atmosphere stratifications as a result of the different velocity adjustment inside the wind farms. For $\Gamma = 1$ K/km (Figure 11a), the power output remains almost constant after the second turbine row in the aligned farm case while it gradually decreases after the third row in the staggered case. The steady power output trend is consistent with the gradual velocity adjustment trend discussed above. For $\Gamma = 5$ K/km (Figure 11b), the power output increases gradually from the 5th turbine row to the 11th row as the mean flow inside the farms slowly accelerates and approaches its fully-developed regime. The power output then becomes steady for both farm configurations from the 12th to the 21st turbine row. The power output of both farm agrees well with that of its infinite counterpart from the 12th turbine row to the 21st row, where the flow inside the wind farm is fully adjusted. As the flow approaches the exit region and begins to accelerate as mentioned above, the power production in both farms also increases quasi linearly from the 22nd row onwards.

4.3. Length of Flow Development Region

In the previous section, it is shown that, under a strong free-atmosphere stratification (i.e., $\Gamma = 5$ K/km), the fully-adjusted flow regime is reached inside the staggered farm at the 12th turbine row, with an adjustment length of 6 km. The fully-developed regime is approached above the farm at the 16th row, with an adjustment distance of 8.5 km. The farm length is 78 times the ABL height, and the adjustment length inside and above the farm is 27 times and 34 times, respectively. However, the flow above the farm does not approach the fully-developed regime under a weak free-atmosphere stratification (i.e., $\Gamma = 1$ K/km), suggesting a longer wind farm is required for the flow to reach such regime. To investigate the adjustment length required for the flow inside and above the farm to reach the fully-developed regime under weak stratification, an additional LES of a staggered large finite-size wind farm with 50 turbine rows under $\Gamma = 1$ K/km is performed, spanning across a streamwise distance of 28 km. The flow above the wind farm reaches the fully-developed regime at the 44th turbine row with an adjustment distance of about 24 km. The wind farm is approximately 102 times of the ABL depth while the adjustment length is approximately 87 times.

The result shows that the conventional assumption proposed by Calaf et al. [2] that fully-developed wind farm flow could be reached for farms whose length exceeds the ABL depth by one order of magnitude underestimates the farm length required as the adjustment length of the simulated farms exceeds the ABL height by two orders of magnitude.

Markfort et al. [61] proposed a canopy-type model similar to that of Belcher et al. [43], which uses scaling analysis to estimate the adjustment length required for flows to transition to the fully-developed regime in neutral ABLs without free-atmosphere stratification. Markfort et al. [61] stated that the streamwise distance necessary for the flow to approach the fully-developed regime could be estimated by the wind farm characteristic drag length, which is defined as

$$L_c = 8z_h \frac{s_x s_y}{\pi C_T}, \tag{9}$$

where z_h is the turbine top-tip height and C_T is the turbine thrust coefficient [62]. According to Equation (9), $L_c \approx 20$ km if $s_x = 7$, $s_y = 7$, $z_h = 110$ m and a turbine thrust coefficient of 0.7 is assumed and the effect of free-atmosphere thermal stratification is neglected. The adjustment length obtained from the model shows good agreement with the LES result under weak stratification. However, since the model cannot account for thermal effects, it overestimates the adjustment length required for wind farms under strong stratification. In the future, it would be interesting to extend the model to include the effect of free-atmosphere thermal stratification.

4.4. Wind Farm Wakes

To investigate the effect of the wind farms on the flow downwind, the time- and spanwise-averaged velocity and TKE profiles downwind of the wind farms are examined and shown in Figures 12 and 13, respectively. Under $\Gamma = 1$ K/km, the velocity magnitude 10 km downwind of the wind farm still has 3.6% and 3.4% deficit at hub height for the aligned and staggered cases, respectively. This velocity deficit would result in approximately 10% power loss in a wind turbine installed 10 km downwind from the wind farm. These results demonstrate that the effect of the farm wake could be far-reaching, and sufficient spacing between wind farms is required to minimize the potential power losses associated with wind farm wakes.

For the cases under $\Gamma = 5$ K/km, a relatively fast wake recovery is observed as the flow in the rotor region recovers to its inflow at 5 km downwind of the wind farm. As discussed in Section 4.2, the farm flow accelerates in the exit region, which extends several kilometers upwind of the farm trailing edge. The advantageous pressure gradient generated continues downwind of the wind farm. Because of the favorable pressure gradient, the farm wake recovers significantly faster under $\Gamma = 5$ K/km than under $\Gamma = 1$ K/km.

In regards to the TKE within the rotor region, it returns to its inflow magnitude 10 km downwind of the farm for the cases under $\Gamma = 1$ K/km. This is consistent with the faster recovery of the turbulence compared to the mean flow previously reported downwind of roughness transitions. Under $\Gamma = 5$ K/km, the TKE recovers to its inflow magnitude 5 km downwind of the farms. It is worth noticing that the TKE above the farm top-tip level is still higher than its inflow magnitude even though the TKE within the rotor region has returned to its inflow magnitude for all the cases considered.

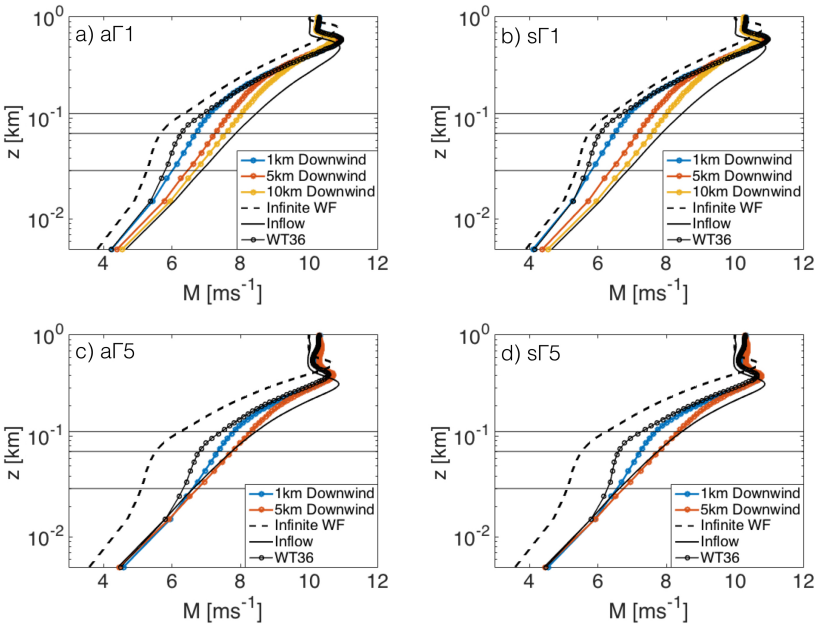

Figure 12. Vertical profiles of time- and spanwise-averaged velocity magnitude at 1 km, 5 km and 10 km downwind of the wind farm, and at the 36th (last) turbine row for the cases: (**a**) FS-aΓ1; (**b**) FS-sΓ1; (**c**) FS-aΓ5; and (**d**) FS-sΓ5. The solid black profile represents the velocity magnitude of the ABL inflow, and the black dashed profile represents the time- and horizontal-averaged velocity magnitude of the infinite wind farm with the same wind farm configuration. The black horizontal solid lines represent the top-tip, hub and bottom-tip heights.

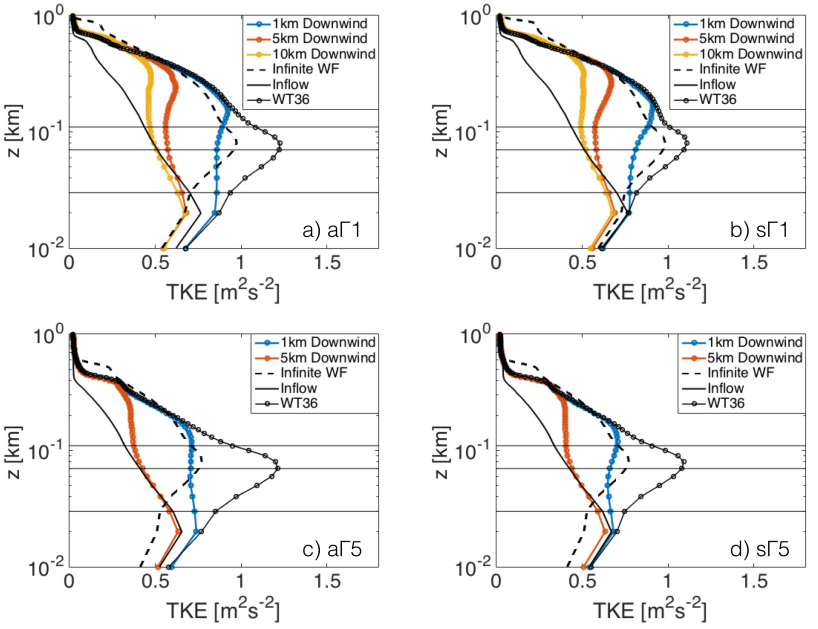

Figure 13. Vertical profiles of time- and spanwise-averaged TKE at 1 km, 5 km and 10 km downwind of the wind farm, and at the 36th (last) turbine row for the cases: (**a**) FS-aΓ1; (**b**) FS-sΓ1; (**c**) FS-aΓ5; and (**d**) FS-sΓ5. The solid black profile represents the TKE of the ABL inflow, and the black dashed profile represents the time- and horizontal-averaged total shear stress of the infinite wind farm with the same turbine configuration. The black horizontal solid lines represent the top-tip, hub and bottom-tip heights.

5. Summary

The present work investigates the CNBL flow adjustment inside and around large finite-size wind farms with aligned and staggered layouts under two free-atmosphere stratification levels, $\Gamma = 1$ K/km and $\Gamma = 5$ K/km. The flow adjustment inside and around the wind farms is studied within the following flow regions: (1) the induction region; (2) the entrance and development region; (3) the fully-developed region; (4) the exit region, and (5) the farm wake region.

The induction region upstream of the wind farms under weak free-atmosphere stratification ($\Gamma = 1$ K/km), induced by the cumulative turbine blockage effect, extends about 0.8 km and leads to a velocity deficit of 0.8% and 1.2% at a distance of 2.5 D rotor diameters upwind of the aligned and staggered wind farms, respectively. This, in turn, leads to a power deficit of 1.3% and 3% at the first row of turbines. Under $\Gamma = 5$ K/km, a 10% and 11% velocity deficit is observed for the aligned and staggered cases, respectively, and results in a power reduction of 36% and 41% at the first turbine row. The induction region in both farm layouts extends 7 km upwind of the wind farm. The decrease in the power output of the first turbine row is more than 35% in both farm configurations, compared to the cases under $\Gamma = 1$ K/km.

The large difference in the size and impact of the induction region associated with the change in free-atmosphere stratification can be explained by the fact that the flow is subcritical ($Fr < 1$) for $\Gamma = 5$ K/km, while it is supercritical ($Fr > 1$) for $\Gamma = 1$ K/km. The upward displacement of the subcritcal flow at the farm leading edge triggers gravity waves and associated pressure disturbances which propagate upwind under $\Gamma = 5$ K/km. A high-pressure region is generated at the farm entrance, leading to a gravity wave-induced blockage effect and a substantial deceleration of the flow upwind of the wind farm. The staggered wind farm configuration is shown to cause a stronger wave-induced blockage effect than the aligned configuration. The impact of the induction region on the flow and the performance of the wind farm highlights the importance of accounting for such effect when predicting wind farm performance.

In the entrance and development region, the flow decelerates due to wind turbine momentum extraction, leading to an IBL growth above the wind farm. It is shown that, if the wind farm is large enough along the streamwise direction, the IBL of the wind farm interacts with the ABL above and displaces it upward. The wind farm flow adjusts towards the infinite wind farm regime faster under a stronger stratification. For the cases under $\Gamma = 1$ K/km, the flow inside and above both wind farms, and thus the turbine power production, do not approach the fully-developed regime even though the farm length is two orders of magnitude larger than the ABL height. This is in contrast to the common assumption that the flow becomes fully developed over wind farms whose lengths are one order of magnitude larger than the ABL height. Under $\Gamma = 5$ K/km, the overall mean flow of the staggered farm, and thus the turbine power, approach the fully-developed regime at around 8.5 km downwind of the farm leading edge; however, the flow above the aligned farm does not approach its fully-developed regime due to the flow heterogeneity caused by the presence of high-speed channels between the turbine columns.

As the flow approaches the trailing edge of the farm, under strong free-atmosphere stratification ($\Gamma = 5$ K/km), the flow accelerates in the so-called the exit region, leading to a quasi-linear increase in power production in both farms. This can be explained by the fact that, at the trailing edge of the wind farms, there is a downward mean flow component that triggers gravity waves and a low-pressure region under subcritical flow conditions. Similar to the phenomenon in the induction region, the gravity waves and the low-pressure region propagate upwind from the trailing farm edge. This results in an advantageous pressure gradient, which accelerates the flow and leads to a power increase at the exit region of the wind farms. The region extends 7 km upwind from the wind farm trailing edge, similar to the length of the induction region. The flow acceleration and increase in power production are not observed in the cases under $\Gamma = 1$ K/km, as the flow is supercritical and no upwind propagating gravity waves can be triggered.

Free-atmosphere thermal stratification is shown to have a strong effect also on the structure and recovery of the wind farm wakes. Velocity deficits of about 3.5% are observed 10 km downwind of both wind farms for $\Gamma = 1$ K/km, implying a potential 10% loss in power output if a turbine is installed at that distance downwind. The TKE at the rotor height level has returned to its inflow condition 10 km downwind of the farm. On the other hand, under $\Gamma = 5$ K/km, both the velocity and TKE at the rotor height level have returned to their inflow levels 5 km downwind from the wind farm. As more large wind farms are planned to be installed in close proximity to other farms, these results provide insight into the potential power loses associated with wind farm wakes under different free-atmosphere thermal stratification.

Future research will focus on the effects of different atmospheric surface layer and free-atmosphere stabilities on the performance of large wind farms that are finite in both streamwise and spanwise directions. The effects on land-atmosphere exchanges of momentum and scalars will also be examined.

Acknowledgments: This research was supported by the Swiss National Science Foundation (Grant 200021_172538), the Swiss Federal Office of Energy (Grant SI/501337-01) and the Swiss Innovation and Technology Committee (CTI) within the context of the Swiss Competence Center for Energy Research "FURIES: Future Swiss Electrical Infrastructure". Computing resources were provided by the Swiss National Supercomputing Centre (CSCS) under Project ID s706.

Author Contributions: This study was done as part of Ka Ling Wu's doctoral studies supervised by Fernando Porté-Agel.

Conflicts of Interest: The authors declare no conflict of interest.

References

1. Frandsen, S.; Barthelmie, R.; Pryor, S.; Rathmann, O.; Larsen, S.; Højstrup, J.; Thøgersen, M. Analytical modelling of wind speed deficit in large offshore wind farms. *Wind Energy* **2006**, *9*, 39–53.
2. Calaf, M.; Meneveau, C.; Meyers, J. Large eddy simulation study of fully developed wind-turbine array boundary layers. *Phys. Fluids* **2010**, *22*, 015110.
3. Meyers, J.; Meneveau, C. Large eddy simulations of large wind-turbine arrays in the atmospheric boundary layer. In Proceedings of the 48th AIAA Aerospace Sciences Meeting Including the New Horizons Forum and Aerospace Exposition, Orlando, FL, USA, 4–7 January 2010.
4. Lu, H.; Porté-Agel, F. Large-eddy simulation of a very large wind farm in a stable atmospheric boundary layer. *Phys. Fluids* **2011**, *23*, 065101.
5. Meyers, J.; Meneveau, C. Optimal turbine spacing in fully developed wind farm boundary layers. *Wind Energy* **2012**, *15*, 305–317.
6. Johnstone, R.; Coleman, G.N. The turbulent Ekman boundary layer over an infinite wind-turbine array. *J. Wind Eng. Ind. Aerodyn.* **2012**, *100*, 46–57.
7. Abkar, M.; Porté-Agel, F. The effect of free-atmosphere stratification on boundary-layer flow and power output from very large wind farms. *Energies* **2013**, *6*, 2338–2361.
8. Calaf, M.; Parlange, M.B.; Meneveau, C. Large eddy simulation study of scalar transport in fully developed wind-turbine array boundary layers. *Phys. Fluids* **2011**, *23*, 126603.
9. VerHulst, C.; Meneveau, C. Large eddy simulation study of the kinetic energy entrainment by energetic turbulent flow structures in large wind farms. *Phys. Fluids* **2014**, *26*, 025113.
10. Abkar, M.; Porté-Agel, F. Mean and turbulent kinetic energy budgets inside and above very large wind farms under conventionally-neutral condition. *Renew. Energy* **2014**, *70*, 142–152.
11. Porté-Agel, F.; Wu, Y.T.; Lu, H.; Conzemius, R. Large-eddy simulation of atmospheric boundary layer flow through wind turbines and wind farms. *J. Wind Eng. Ind. Aerodyn.* **2011**, *99*, 154–168.
12. Porté-Agel, F.; Wu, Y.T.; Chen, C.H. A numerical study of the effects of wind direction on turbine wakes and power losses in a large wind farm. *Energies* **2013**, *6*, 5297–5313.
13. Wu, Y.T.; Porté-Agel, F. Simulation of turbulent flow inside and above wind farms: Model validation and layout effects. *Bound.-Layer Meteorol.* **2013**, *146*, 181–205.
14. Wu, Y.T.; Porté-Agel, F. Modeling turbine wakes and power losses within a wind farm using LES: An application to the Horns Rev offshore wind farm. *Renew. Energy* **2015**, *75*, 945–955.

15. Allaerts, D.; Meyers, J. Effect of inversion-layer height and Coriolis forces on developing wind-farm boundary layers. In Proceedings of the 34th Wind Energy Symposium, San Diego, CA, USA, 4–8 January 2016; p. 1989.
16. Ivanell, S. Numerical Computations of Wind Turbine Wakes. Ph.D. Thesis, Gotland University, Visby, Sweden, 2009.
17. Churchfield, M.J.; Lee, S.; Moriarty, P.J.; Martinez, L.A.; Leonardi, S.; Vijayakumar, G.; Brasseur, J.G. A large-eddy simulation of wind-plant aerodynamics. In Proceedings of the 50th AIAA Aerospace Sciences Meeting Including the New Horizons Forum and Aerospace Exposition, Aerospace Sciences Meetings, Nashville, TN, USA, 9–12 January 2012.
18. Eriksson, O.; Lindvall, J.; Breton, S.P.; Ivanell, S. Wake downstream of the Lillgrund wind farm-A Comparison between LES using the actuator disc method and a Wind farm Parametrization in WRF. *J. Phys. Conf. Ser.* **2015**, *625*, 012028.
19. Nilsson, K.; Ivanell, S.; Hansen, K.; Mikkelsen, R.; Sørensen, J.; Breton, S.P.; Henningson, D. Large-eddy simulations of the Lillgrund wind farm. *Wind Energy* **2015**, *18*, 449–467.
20. Abkar, M.; Sharifi, A.; Porté-Agel, F. Wake flow in a wind farm during a diurnal cycle. *J. Turbul.* **2016**, *17*, 420–441.
21. Allaerts, D.; Meyers, J. Boundary-layer development and gravity waves in conventionally neutral wind farms. *J. Fluid Mech.* **2017**, *814*, 95–130.
22. Barthelmie, R.; Hansen, K.; Frandsen, S.; Rathmann, O.; Schepers, J.; Schlez, W.; Phillips, J.; Rados, K.; Zervos, A.; Politis, E.; et al. Modelling and measuring flow and wind turbine wakes in large wind farms offshore. *Wind Energy* **2009**, *12*, 431–444.
23. Creech, A.; Früh, W.G.; Maguire, A.E. Simulations of an offshore wind farm using large-eddy simulation and a torque-controlled actuator disc model. *Surv. Geophys.* **2015**, *36*, 427–481.
24. Ghaisas, N.S.; Archer, C.L.; Xie, S.; Wu, S.; Maguire, E. Evaluation of layout and atmospheric stability effects in wind farms using large-eddy simulation. *Wind Energy* **2017**, *20*, 1227–1240.
25. Barthelmie, R.; Pryor, S.; Frandsen, S.; Hansen, K.; Schepers, J.; Rados, K.; Schlez, W.; Neubert, A.; Jensen, L.; Neckelmann, S. Quantifying the impact of wind turbine wakes on power output at offshore wind farms. *J. Atmos. Ocean. Technol.* **2010**, *27*, 1302–1317.
26. Zilitinkevich, S.; Baklanov, A.; Rost, J.; Smedman, A.S.; Lykosov, V.; Calanca, P. Diagnostic and prognostic equations for the depth of the stably stratified Ekman boundary layer. *Q. J. R. Meteorol. Soc.* **2002**, *128*, 25–46.
27. Nygaard, N.G. Wakes in very large wind farms and the effect of neighbouring wind farms. *J. Phys. Conf. Ser.* **2014**, *524*, 012162.
28. Jensen, N.O. *A Note on Wind Generator Interaction*; Risø National Laboratory: Roskilde, Denmark, 1983.
29. Bleeg, J.; Traiger, E.; Purcell, M.; Landberg, L. Wind farm blockage and its impact on energy production. In Proceedings of the Wind Energy Science Conference 2017, Lyngby, Denmark, 26–29 June 2017.
30. Porté-Agel, F.; Meneveau, C.; Parlange, M. A scale-dependent dynamic model for large-eddy simulation: Application to a neutral atmospheric boundary layer. *J. Fluid Mech.* **2000**, *415*, 261–284.
31. Porté-Agel, F. A scale-dependent dynamic model for scalar transport in large-eddy simulations of the atmospheric boundary layer. *Bound.-Layer Meteorol.* **2004**, *112*, 81–105.
32. Stoll, R.; Porté-Agel, F. Dynamic subgrid-scale models for momentum and scalar fluxes in large-eddy simulations of neutrally stratified atmospheric boundary layers over heterogeneous terrain. *Water Resour. Res.* **2006**, *42*, doi:10.1029/2005WR003989.
33. Wu, Y.T.; Porté-Agel, F. Large-eddy simulation of wind-turbine wakes: Evaluation of turbine parametrisations. *Bound.-Layer Meteorol.* **2011**, *138*, 345–366.
34. Albertson, J.; Parlange, M. Surface length scales and shear stress: Implications for land-atmosphere interaction over complex terrain. *Water Resour. Res.* **1999**, *35*, 2121–2132.
35. Orszag, S. Transform method for the calculation of vector-coupled sums: Application to the spectral form of the vorticity equation. *J. Atmos. Sci.* **1970**, *27*, 890–895.
36. Canuto, C.; Hussaini, M.Y.; Quarteroni, A.M.; Thomas, A., Jr. *Spectral Methods in Fluid Dynamics*; Springer Science & Business Media: Berlin, Germany, 2012.
37. Stoll, R.; Porté-Agel, F. Surface heterogeneity effects on regional-scale fluxes in stable boundary layers: Surface temperature transitions. *J. Atmos. Sci.* **2009**, *66*, 412–431.
38. Moeng, C.H. A large-eddy-simulation model for the study of planetary boundary-layer turbulence. *J. Atmos. Sci.* **1984**, *41*, 2052–2062.

39. Abkar, M.; Porté-Agel, F. A new boundary condition for large-eddy simulation of boundary-layer flow over surface roughness transitions. *J. Turbul.* **2012**, *13*, doi:10.1080/14685248.2012.695077.
40. Hansen, K.S.; Barthelmie, R.J.; Jensen, L.E.; Sommer, A. The impact of turbulence intensity and atmospheric stability on power deficits due to wind turbine wakes at Horns Rev wind farm. *Wind Energy* **2012**, *15*, 183–196.
41. Munters, W.; Meneveau, C.; Meyers, J. Turbulent inflow precursor method with time-varying direction for large-eddy simulations and applications to wind farms. *Bound.-Layer Meteorol.* **2016**, *159*, 305–328.
42. Sescu, A.; Meneveau, C. A control algorithm for statistically stationary large-eddy simulations of thermally stratified boundary layers. *Q. J. R. Meteorol. Soc.* **2014**, *140*, 2017–2022.
43. Belcher, S.; Jerram, N.; Hunt, J. Adjustment of a turbulent boundary layer to a canopy of roughness elements. *J. Fluid Mech.* **2003**, *488*, 369–398.
44. Medici, D.; Ivanell, S.; Dahlberg, J.Å.; Alfredsson, P.H. The upstream flow of a wind turbine: Blockage effect. *Wind Energy* **2011**, *14*, 691–697.
45. Simley, E.; Angelou, N.; Mikkelsen, T.; Sjöholm, M.; Mann, J.; Pao, L.Y. Characterization of wind velocities in the upstream induction zone of a wind turbine using scanning continuous-wave lidars. *J. Renew. Sustain. Energy* **2016**, *8*, 013301.
46. Branlard, E. *Wind Turbine Aerodynamics and Vorticity-Based Methods: Fundamentals and Recent Applications*; Springer: Berlin, Germany, 2017; Volume 7.
47. Queney, P. The problem of air flow over mountains: A summary of theoretical studies. *Bull. Am. Meteorol. Soc.* **1948**, *29*, 16–26.
48. Durran, D.R. Mountain waves and downslope winds. In *Atmospheric Processes Over Complex Terrain*; Springer: Berlin, Germany, 1990; pp. 59–81.
49. Smith, R.B. Gravity wave effects on wind farm efficiency. *Wind Energy* **2010**, *13*, 449–458.
50. Reinecke, P.A.; Durran, D.R. Estimating topographic blocking using a Froude number when the static stability is nonuniform. *J. Atmos. Sci.* **2008**, *65*, 1035–1048.
51. Vosper, S.; Wells, H.; Brown, A. Accounting for non-uniform static stability in orographic drag parametrization. *Q. J. R. Meteorol. Soc.* **2009**, *135*, 815–822.
52. Rominger, J.T.; Nepf, H.M. Flow adjustment and interior flow associated with a rectangular porous obstruction. *J. Fluid Mech.* **2011**, *680*, 636–659.
53. Claussen, M. The flow in a turbulent boundary layer upstream of a change in surface roughness. *Bound.-Layer Meteorol.* **1987**, *40*, 31–86.
54. Belcher, S.E.; Harman, I.N.; Finnigan, J.J. The wind in the willows: Flows in forest canopies in complex terrain. *Annu. Rev. Fluid Mech.* **2012**, *44*, 479–504.
55. Garratt, J. The internal boundary layer—A review. *Bound.-Layer Meteorol.* **1990**, *50*, 171–203.
56. Elliott, W.P. The growth of the atmospheric internal boundary layer. *Trans. Am. Geophys. Union* **1958**, *39*, 1048–1054.
57. Morse, A.; Gardiner, B.; Marshall, B. Mechanisms controlling turbulence development across a forest edge. *Bound.-Layer Meteorol.* **2002**, *103*, 227–251.
58. Shir, C. A numerical computation of air flow over a sudden change of surface roughness. *J. Atmos. Sci.* **1972**, *29*, 304–310.
59. Stevens, R.J.; Gayme, D.F.; Meneveau, C. Large eddy simulation studies of the effects of alignment and wind farm length. *J. Renew. Sustain. Energy* **2014**, *6*, 023105.
60. Porté-Agel, F.; Lu, H.; Wu, Y.T. Interaction between large wind farms and the atmospheric boundary layer. *Procedia IUTAM* **2014**, *10*, 307–318.
61. Markfort, C.D.; Zhang, W.; Porté-Agel, F. Turbulent flow and scalar transport through and over aligned and staggered wind farms. *J. Turbul.* **2012**, *13*, N33.
62. Frandsen, S.T.; Jørgensen, H.E.; Barthelmie, R.; Rathmann, O.; Badger, J.; Hansen, K.; Ott, S.; Rethore, P.E.; Larsen, S.E.; Jensen, L.E. The making of a second-generation wind farm efficiency model complex. *Wind Energy* **2009**, *12*, 445–458.